Title
Electrophoretic Deposition of Mesoporous Niobium(V)Oxide Nanoscopic Films

Journal
Chemistry of Materials, 30(18)

ISSN
0897-4756

Authors
Jha, Gaurav
Tran, Thien
Qiao, Shaopeng
et al.

Publication Date
2018-09-25

DOI
10.1021/acs.chemmater.8b03254

Peer reviewed

CHEMISTRY OF MATERIALS

Article

pubs.acs.org/cm

Electrophoretic Deposition of Mesoporous Niobium(V)Oxide Nanoscopic Films

Gaurav Jha,[†] Thien Tran,[†] Shaopeng Qiao,[†] Joshua M. Ziegler,[†] Alana F. Ogata,[†] Sheng Dai,[‡] Mingjie Xu,[‡] Mya Le Thai,[†] Girija Thesma Chandran,[†] Xiaoqing Pan,*[,‡] and Reginald M. Penner*[,†]

[†]Department of Chemistry, University of California, Irvine, California 92697, United States

[‡]Department of Materials Science and Engineering, University of California, Irvine, California 92697, United States

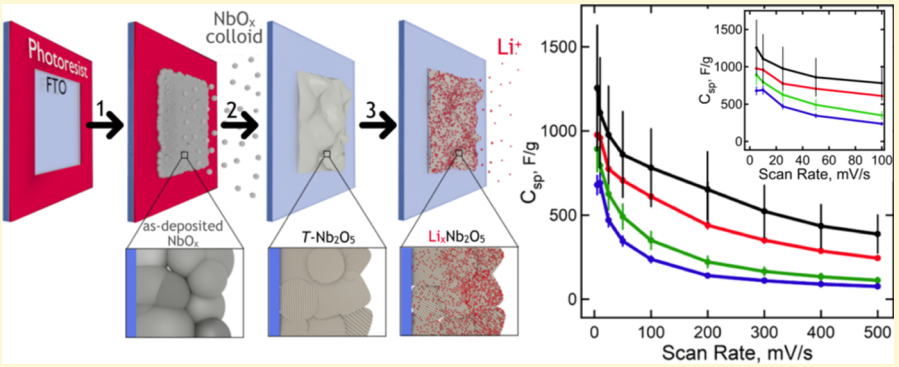

ABSTRACT: Nb_2O_5 is a Li^+ intercalation metal oxide that is of current interest for lithium ion battery electrodes. The electrophoretic deposition (ED) of Nb_2O_5 thin-films from aqueous, NbO_x colloidal solutions is reported here. For films ranging in thickness from 38 to 144 nm, the mass loading of Nb_2O_5 on the electrode is correlated with the coulometry of ED using quartz crystal microbalance gravimetry. Crystalline, phase pure films of orthorhombic, *T*-Nb_2O_5, are obtained by postdeposition calcination. These films exhibit unusually high specific capacities for Li^+-based energy storage as a consequence of ≈70% porosity. For example, a 60 nm thick film displays a specific capacity, C_{sp}, of 420 mAh/g at 5 A/g and 220 mAh/g at 50 A/g, which can be compared with the theoretical Faradaic capacity of 202 mAh/g. *T*-Nb_2O_5 films also have a specific energy density in the range from 770−486 Wh/kg, and a specific power density in the range from 9 to 90 kW/kg. These excellent energy storage metrics are attributed to augmentation of the Faradaic capacity by high double-layer capacities enabled by the mesoporous structure of these films.

INTRODUCTION

Niobium pentoxide, Nb_2O_5, is a Li^+ intercalation material that exhibits intercalation pseudocapacitance as a consequence of the availability of three accessible redox states for Nb centers: Nb^{3+}, Nb^{4+}, and Nb^{5+}.[1−6] The Li^+ insertion/deinsertion reaction is written as

$$Nb_2O_5 + xLi^+ + xe^- \rightleftharpoons Li_xNb_2O_5 \quad (1)$$

where x in the range from 1.6−2.0 has been reported.[7] The intercalation of Li^+ according to reaction 1 causes a color change of the $Li_xNb_2O_5$ which has been investigated for applications in electrochromic coatings.[8−12] Nb_2O_5 is polymorphic, and the three most common polymorphs are *T*-Nb_2O_5 (orthorhombic), *M*-Nb_2O_5 (monoclinic), and *H*-Nb_2O_5 (pseudohexagonal). For Li^+-based energy storage, Dunn and others[2,4,13,14] have demonstrated that orthorhombic niobium pentoxide (*T*-Nb_2O_5) is capable of exhibiting unusually high capacities coupled with rapid charge−discharge rates, as compared with many other transition metal oxides (Table 1). Grey and co-workers[15] have attributed the high rate capability of *T*-Nb_2O_5 to low activation barriers, on the order of a few k_BT, for Li^+ transport in this material, as measured using nuclear magnetic resonance.

T-Nb_2O_5 is most often synthesized by hydrothermal methods,[1,2,4,13,14] and highly dispersed *T*-Nb_2O_5 on carbon has demonstrated specific capacities of up to 590 F/g.[14] Other methods for preparing Nb_2O_5 films include electrospinning followed by thermal annealing,[16] spray pyrolysis,[17] sol−gel processing methods,[9,10,18] electrospinning,[19] and reactive sputtering.[11]

Electrodeposition has hardly been attempted, in spite of the fact that it is an attractive method for both electrochromics and battery/capacitor materials because it promotes an electrically intimate contact with an electrode that can also serve as a current collector. The reason is that electrodeposition of Nb_2O_5 is difficult: the cathodic electrodeposition of niobium oxides (NbO_x) is complicated by the very negative reduction potential for Nb^{3+} (−1.1 V vs NHE) which makes disruptive

Received: August 1, 2018
Revised: August 27, 2018
Published: August 30, 2018

DOI: 10.1021/acs.chemmater.8b03254
Chem. Mater. XXXX, XXX, XXX−XXX

Table 1. Comparison of Observed Photoelectron Binding Energies For Nb_2O_5 Films With Literature Values

compound	binding energy (eV) Nb $3d_{5/2}$	Nb $3d_{3/2}$	O 1s	Nb:O[a]	reference
T-Nb_2O_5 (SG, d = 120 nm)	207.3	210.1	530.6	0.40	18
Nb_2O_5 (Nb^o TO)	207.7	210.4	530.4	0.46	8
B-Nb_2O_5	207.1	209.8	530	n.a.	44
a-Nb_2O_5 (MS-ad, d = 377 nm)	207.4	210.1	530.5	0.40	12
Nb_2O_5-600 °C (MS-ta, d = 355 nm)	207.1	209.9	530.1	0.40	12
ED (this work)					
a-Nb_2O_5 (d = 50 nm)	207.5	210.2	530.5	0.40	this work
T-Nb_2O_5 (d = 50 nm)	207.2	209.9	530.1	0.43	this work

[a]Nb:O atomic ratio. [b]Abbreviations: SG = sol–gel, TO = thermal oxidation in air at 580 °C, MS-ad = magnetron sputtering (as-deposited), and MS-ta = magnetron sputtering (calcined at 600 °C).

H_2 coevolution unavoidable in aqueous solutions. Crayston and co-workers[20] circumvented this issue by electrodepositing NbO_x by the precipitation of niobium ions, immobilized in a thin porous film prepared using sol–gel methods, using electrogenerated OH^-. Zhitomirsky[21] reported an aqueous cathodic electrophoretic deposition technique for the preparation of Nb_2O_5 films on Pt electrodes. The mechanism they proposed is based upon the peroxo-precursor method used for titania deposition.[22] Both titanium and niobium salts react promptly with water to form precipitates, but dissolution of the precursor salt in dilute hydrogen peroxide at low temperature (≈ 2 °C) allows for the formation of a stable peroxocation, thought to be $Nb(OH)_4(H_2O_2)^+$ or $NbO_2(H_2O_2)^+$.[21] This complex is hydrolyzed by electrogenerated OH^- at the cathode formed, for example, by H_2 evolution to produce Nb_2O_5.[21] The work of Crayston et al.[20] and Zhitomirsky provide the only precedents for Nb_2O_5 electrodeposition, to our knowledge. However, Nb_2O_5 films have also been obtained by the anodization of electrodeposited niobium metal films,[23] which can be prepared by electrodeposition from molten salts[24] and propylene carbonate or acetonitrile using $LiNbF_6$ as a precursor.[25]

In this work, we describe a robust method for the electrophoretic deposition (ED) of *T*-Nb_2O_5 from NbO_x colloids. NbO_x colloids were obtained using a modification of the Zhitomirsky method,[21] involving the rapid injection of niobium salt dissolved in methanol into a cold (≈ 2 °C) hydrogen peroxide solution. Phase pure *T*-Nb_2O_5 films, with thicknesses varying from 38 to 144 nm, are obtained after calcination at 550 °C. The gravimetric specific capacity of these films exceeds the theoretical Faradaic capacity (202 mAh/g) and capacitance values (403 F/g, 1.8 V window) expected for Nb_2O_5, due to significant contributions from double-layer capacitance. The wetted surface area of these films is increased by a porosity of 64–72% that forms when H_2 bubbles formed during ED are adsorbed and trapped on the nascent Nb_2O_5 surface. The *T*-Nb_2O_5 films prepared by ED retain up to 70% capacity for 5000 charge–discharge cycles.

EXPERIMENTAL METHODS

Chemicals and Materials. Niobium pentachloride ($NbCl_5$, 99%), hydrogen peroxide solution (H_2O_2, 30% (w/w) in H_2O), lithium perchlorate ($LiClO_4$, battery grade, dry, 99.99% trace metal basis), propylene carbonate (anhydrous, 99.7%), and fluorine-doped tin oxide (FTO) coated glass slide (surface resistivity ≈ 3 Ω/sq) were all used as received from Sigma-Aldrich. FTO was cleaned using a commercial cleaning solution Hellmanex 3 obtained from Hellma Analytics. Positive photoresist (Shipley S1808) and developer (Shipley MF-319) were purchased from Microchem Corporation. Acetone and methanol were used as received from Fisher (ACS certified).

Electrophoretic Deposition of Nb_2O_5. An aqueous colloidal solution of Nb_2O_5 nanoparticles was prepared as follows:[21] 135 mg $NbCl_5$ was dissolved in 4 mL methanol and rapidly injected into 96 mL of 0.052 M H_2O_2 at ≈2 °C, resulting in a clear colloidal solution. The solution was aged at room temperature for 3 h at RT before ED. Colloid solutions were discarded 10 h after the rapid injection process.

After cleaning (Hellmanex 3 solution for 5 min, Millipore water rinse, air-dry), 2 × 1 cm FTO glasses were masked with a positive photoresist layer (Shipley S1808). This was spin-coated at 2500 rpm for 80 s onto the FTO, soft baked at 90 °C for 30 min, and patterned to produce a square 6 × 6 mm FTO exposed region (Figure 1a). f1

ED was carried out in a 100 mL one compartment two-electrode electrochemical cell, using a Gamry Series G 300 potentiostat. The working electrode was the patterned FTO surface, which was immersed into the aqueous colloidal solution of Nb_2O_5 nanoparticles, leaving the top edge of the FTO outside the solution for contact with the potentiostat. A platinum foil (1 × 2 cm) counter electrode was positioned at a 2 cm distance from the center of the exposed FTO surface. The deposition was conducted at constant potential of −2.0 V, until the required charge was deposited, as shown in Figure 1g. After deposition, all photoresist was removed using acetone and the sample was air-dried. The sample was heated on a 4 °C/min ramp to 550 °C and was annealed at this temperature for 6 h, followed by a cool-down.

Electrochemical Characterization. All electrochemical measurements were performed by a one-compartment three-electrode cell using a Gamry Series G 300 potentiostat. Cyclic voltametry and galvanostatic measurements were conducted in 1.0 M $LiClO_4$ (battery grade, dry, 99.99%) in dry propylene carbonate inside a N_2 glovebox. 1 ×1 cm Pt foil was used as a unter electrode with a Ag/Ag^+ nonaqueous reference electrode (10 mM Ag^+, DMSO) for the electrochemical measurements. All potentials are quoted with respect to the Li/Li^+ couple, E_{Li/Li^+} = −3.045 V versus normal hydrogen electrode[26] by calibrating the Ag/Ag^+ reference electrode against Li/Li^+ using ferrocene/ferrocenium ($Fc/Fc^{+\bullet}$) in 1 M $LiClO_4$, PC.[27]

Quartz Crystal Microbalance (QCM) Gravimetry. The mass of the Nb_2O_5 deposited by ED was directly determined using QCM. The QCM measurements were performed with a Stanford Research Systems (SRS) QCM200 Quartz Crystal Microbalance Digital Controller, in conjunction with a QCM25 5 MHz Crystal Oscillator equipped with an Au-coated 5 MHz quartz crystal (area = 1.37 cm^2). QCM measures the mass deposited onto the quartz/Au electrode by correlating it to the change in frequency, Δf, according to the Sauerbrey equation.[28]

$$\Delta f = C_f \times \Delta m \quad (2)$$

The sensitivity factor (C_f) of the immersed quartz/gold electrode was calibrated by galvanostatically electrodepositing silver from aqueous 0.5 M $AgNO_3$ + 0.5 M HNO_3 solution, following previously reported methods.[29,30] The C_f value obtained for silver deposition was 47.7(±0.8) Hz cm^2 μg^{-1}. QCM crystals were cleaned by immersion into piranha solution 3:1, conc H_2SO_4:H_2O_2(30%) for 5 min, rinsing in water, air drying, and then 2 h vacuum drying. The initial frequency of the pristine crystal was recorded in air, immediately after vacuum drying. The electrode holder containing the crystal was then immersed in the colloidal NbO_x solution for deposition. After

DOI: 10.1021/acs.chemmater.8b03254
Chem. Mater. XXXX, XXX, XXX–XXX

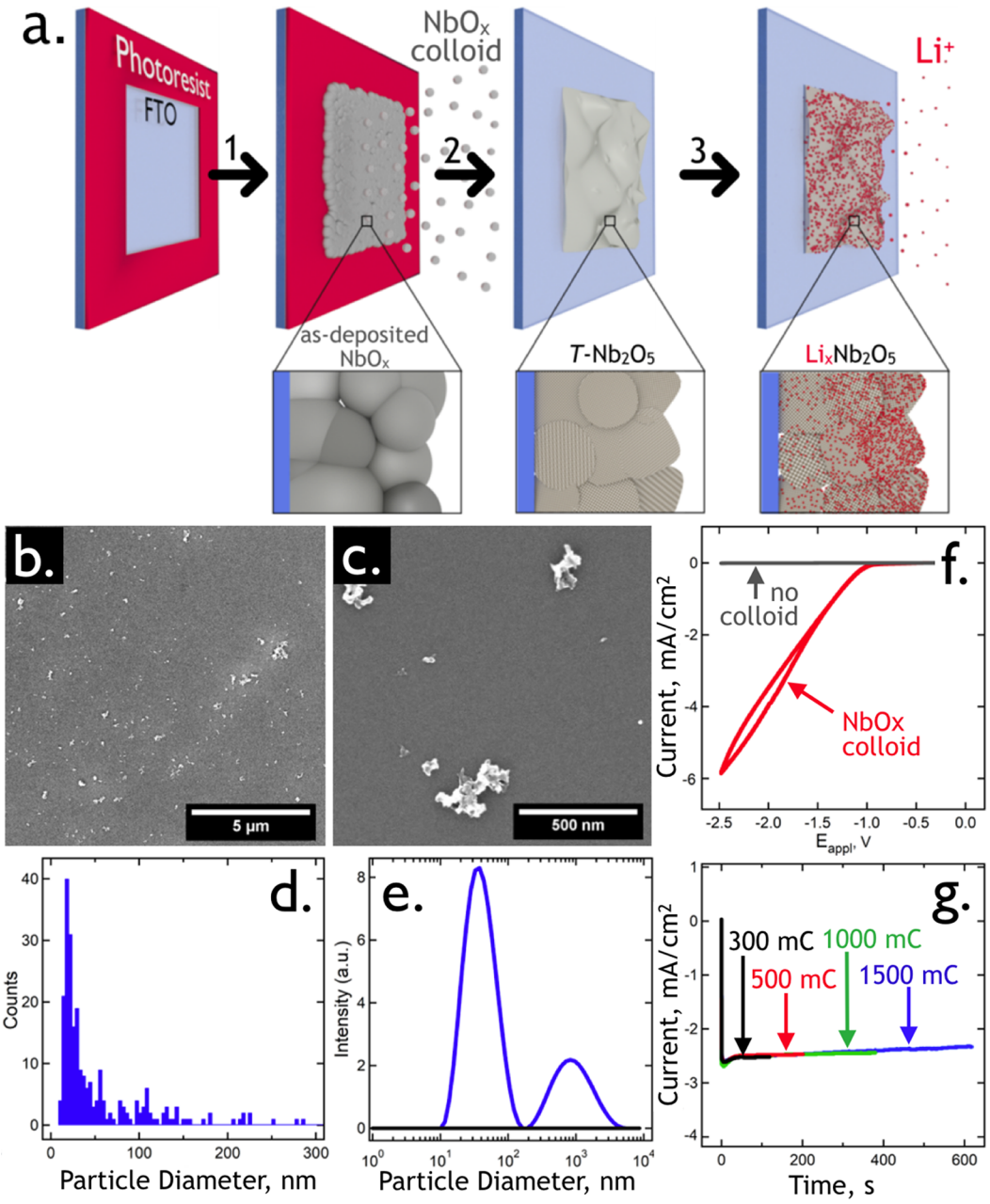

Figure 1. Electrophoretic deposition (ED) of T-Nb_2O_5 film. (a). Three-step process flow: starting with a masked FTO-coated glass (left) electrode with area, 6 × 6 mm area (0.36 cm^2), in step 1 potentiostatic ED is carried out from a colloidal NbO_x solution using two electrodes (FTO-glass and counter electrode). The deposited Nb_2O_5 film is amorphous. In step 2, this a-Nb_2O_5 film is calcined at 550 °C for 5 h, producing T-Nb_2O_5. In step 3, Li^+ can be reversibly intercalated into this T-Nb_2O_5 film. (b) SEM image of drop-cast NbO_x colloid particles on a clean silicon wafer, showing a dispersion of submicron particles. (c) Lower magnification SEM images showing several larger, 500−100 nm diameter colloid particles. (d) SEM-derived particle diameter histogram of NbO_x colloid particles showing the smaller mode, at ≈20 nm, seen in the dynamic light scattering (DLS) fractogram in (e). (e) DLS fractogram showing a bimodal distribution of NbO_x colloid particles. (f) Cyclic voltammograms (2 electrode) at 50 mV/s of aqueous 50 mM H_2O_2 (gray trace) and the colloidal NbO_x solution described above (red trace). (g) Current vs time plots for potentiostatic ED at −2.0 V (two electrode mode). Four plots are overlaid in this plot, corresponding to four Coulombic loadings as indicted, demonstrating the remarkable reproducibility of the ED process.

deposition, the crystal was removed from the holder, rinsed with water, air-dried, and vacuum-dried for 2 h. After drying, the crystal was remounted on the QCM controller to record the change in frequency for the dried sample after deposition. Mean mass versus mean charge produced a slope of 6.18 μg/C, which was used to calculate the dry mass of the ED thin film (see below).

Structural Characterization. Scanning electron micrographs (SEMs) were acquired using a FEI Magellan 400 XHR system. Before imaging, samples were sputter-coated with ≈2 nm of iridium. Accelerating voltages of incident electron beams ranged from 5 to 15 kV, and probe currents ranged from 25 pA to 0.4 nA. All SEM specimens were mounted on stainless stubs and held by carbon tape. Grazing-incidence X-ray diffraction (GIXRD) patterns were obtained using a Rigaku SmartLab X-ray diffractometer employing the parallel beam optics. The X-ray generator was operated at 40 kV and 44 mA with Cu Kα irradiation. X-ray photoelectron spectroscopy (XPS) was measured using the AXIS Supra by Kratos Analytical Inc. equipped with monochromatic Al/Ag X-ray source.

DOI: 10.1021/acs.chemmater.8b03254
Chem. Mater. XXXX, XXX, XXX−XXX

Transmission Electron Microscopy. Aberration-corrected scanning transmission electron microscopy (STEM) was performed on a JEOL Grand-ARM transmission electron microscope equipped with two spherical aberration correctors and a 300 kV cold field emission gun. High-angle annular dark field (HAADF)-STEM images were recorded using a convergence semi angle of 22 mrad and inner- and outer collection angles of 83 and 165 mrad, respectively.

RESULTS AND DISCUSSION

Electrophoretic Deposition of Nb_2O_5 Thin Films. In the cathodic electrodeposition described by Zhitomirsky,[21] the aging of the peroxocation solution for 3 days induces cloudiness and sedimentation in the solution; a consequence of the formation of micron-sized NbO_x particles. We found that such solutions yielded inconsistent results. To resolve this, NbO_x colloid solutions were obtained by rapidly injecting 125 mM $NbCl_5$ in methanol into 52 mM H_2O_2 in water at ≈2 °C. This colloidal solution was then aged for 3 h at RT. The resulting NbO_x particles can be directly observed and measured by scanning electron microscopy (SEM) after drop-casting the colloid solution onto a silicon wafer (Figure 1, panels b and c). These colloids are mainly in the diameter range from 20 to 30 nm (Figure 1d), but larger colloids extending to 1.0 μm are also seen in these solutions (Figure 1, panels b and c). The SEM analysis of these particles is supported by dynamic light scattering (DLS) data (Figure 1e) that shows two prominent modes at ≈20 nm and 1.0 μm.

Cyclic voltammograms (2 electrode) of the FTO-glass working electrode in aqueous H_2O_2 (pH = 7.0) shows virtually no Faradaic current, but in the presence of NbO_x colloid (pH = 5.0), a reduction is observed that is attributed to migration of the positively charged NbO_x colloids and H_2 evolution (HER) coupled with ED of the NbO_x colloid (Figure 1f). Potentiostatic ED at −2 V rapidly produces a steady-state current of 2.5 mA/cm^2 (Figure 1g) that decreases gradually with time. ED current versus time data traces for four experiments actually overlay one another (Figure 1g), demonstrating the reproducibility of this process. Samples were prepared using one of four total charge values, Q_{dep}: 300, 500, 1000, and 1500 mC. It should be emphasized that Q_{dep} encompasses both the charge associated with HER and that of ED.

Structural and Compositional Characterization. SEM images of as-deposited NbO_x films (Figure 2, panels a and c) show a mud-cracked topography and some texturing of the film surface on the ≈100 nm size scale. These cracks can be attributed to dry shrinkage, as previously reported for Nb_2O_5 films prepared for electrochromic applications,[31] caused by the contraction of metal oxides upon loss of capillary water. After calcination, deep cracks become filled and a smoother topography is seen for the film surface (Figure 2, panels d–f).

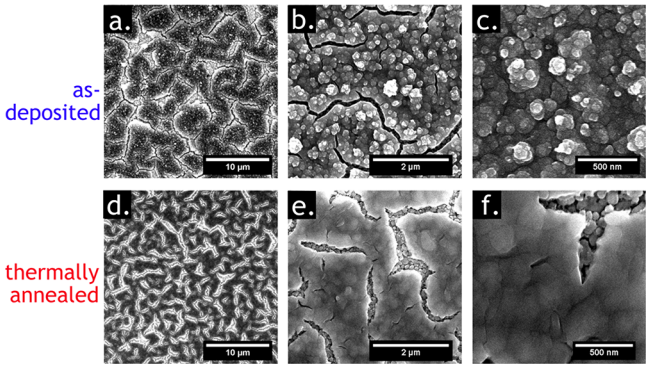

Figure 2. Scanning electron microscopy (SEM). (a–c) As-deposited NbO_x films at three magnifications, and (d–f) T-Nb_2O_5 films after calcination at 550 °C for 5 h.

A cross-sectional STEM image of a T-Nb_2O_5 film at low magnification shows several of these cracks (Figure 3a). Energy dispersive X-ray spectroscopy (EDS) elemental maps (Figure 3a, bottom) confirm the T-Nb_2O_5 region, labeled in the STEM cross section. At higher magnification, the crystallinity of the T-Nb_2O_5 layer is revealed in atomic-resolution STEM images (Figure 3b). In this image, (181) and (18-1) planes are observed together with a measured d-spacing of 2.45 Å. Defects are also observed in these layers, as seen for example in Figure 3c where a white dashed-line marks a grain boundary confirming the polycrystalline structure of the ED-deposited T-Nb_2O_5 layer.

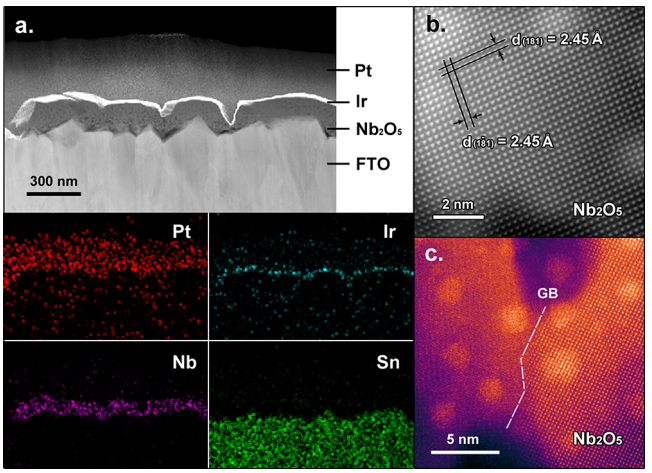

Figure 3. Cross-sectional TEM for AC-STEM characterization of T-Nb_2O_5 sample. (a) Cross-section view of a T-Nb_2O_5 on FTO. EDS elemental maps confirm the presence of Nb in the T-Nb_2O_5 region. Pt and Ir protecting layers were deposited for the TEM sample preparation. (b) Atomic-resolution STEM image of the T-Nb_2O_5 layer showing characteristic $d_{(181)}$-spacings of 2.45 Å. (c) STEM image of the T-Nb_2O_5 layer showing a grain boundary, confirming its polycrystalline structure.

The surface chemical composition of ED-as-deposited NbO_x films and T-Nb_2O_5 films were assessed by XPS (Figure 4, panels a and b, and Table 1). As-prepared films showed binding energies (B.E.) for Nb $3d_{5/2}$, Nb $3d_{3/2}$, and O 1s at 207.5, 210.3, and 530.5 eV, respectively, all within 0.1 eV of the B.E. reported for amorphous Nb_2O_5 (Table 1).[12] The Nb:O stoichiometry of these films was 0.40, also as previously reported.[12] B.E. values of Nb $3d_{5/2}$, $3d_{3/2}$ peaks for calcined films slightly decreased to 207.4 and 210.2 eV (Figure 4a), respectively, while O 1s at 530.4 eV decreased by 0.2 eV (Figure 4b). Similar B.E. decreases for metal oxides have been attributed to a decrease in the bandgap of the oxide caused by the creation of oxygen vacancies during annealing.[12] The O 1s photoelectron envelope can be deconvoluted into a lower B.E. component assigned to niobium oxide (≈ 532.2 eV), and the higher B.E. component (530.5 eV) assigned to $OH^{\bullet}$ and peroxocomplex species which contribute a significant shoulder on the low B.E. side of the O 1s.[12] However, these species decompose upon calcination leading to a dramatic reduction in the intensity of this shoulder (Figure 4b).

DOI: 10.1021/acs.chemmater.8b03254
Chem. Mater. XXXX, XXX, XXX−XXX

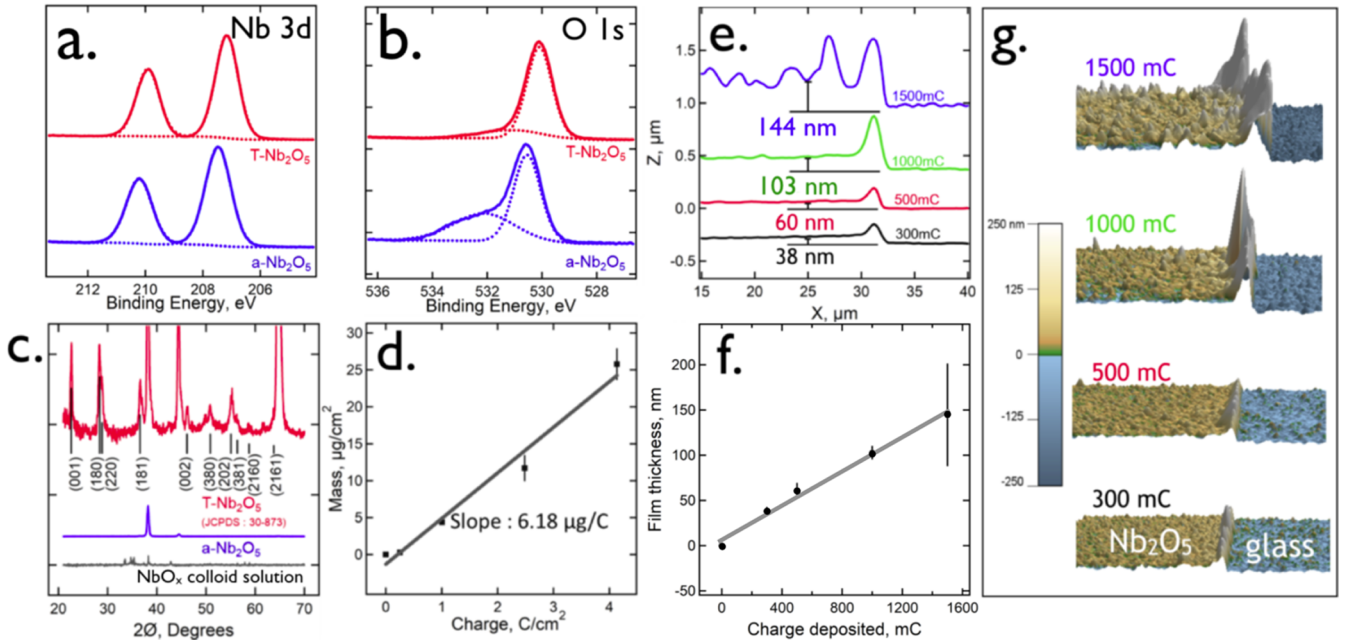

Figure 4. *T*-Nb_2O_5 film characterization. (a and b) High-resolution XPS spectra of 500 mC *T*-Nb_2O_5 and a-Nb_2O_5 films. The observed chemical shifts are compared with literature values in Table 1. (c) Powder XRD patterns for as-deposited Nb_2O_5, a-Nb_2O_5, and *T*-Nb_2O_5, as indicated. (d) QCM measurements of the deposited Nb_2O_5 mass as a function of deposition charge. (e) AFM amplitude traces for four *T*-Nb_2O_5 films, prepared using 300, 500, 1000, and 1500 mC, as indicated. (f) AFM-measured film thickness as a function of deposition charge. (g) AFM images of film edges for the same four deposition charges shown in (e).

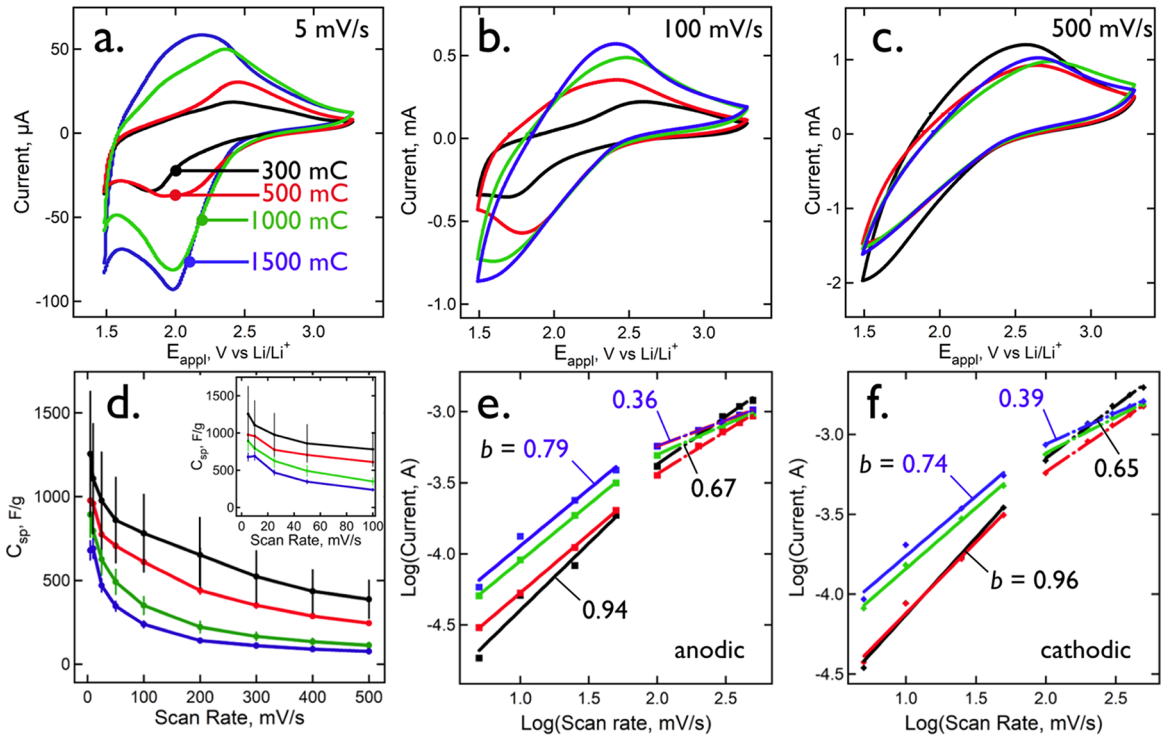

Figure 5. Cyclic voltammetry (CV) of *T*-Nb_2O_5 films. (a–c) CVs at scan rates of (a) 5, (b) 100, and (c) 500 mV/s, for *T*-Nb_2O_5 films prepared using four Q_{dep} values as indicated. (d) Specific capacity, C_{sp}, calculated from the CVs like those of (a–c). Error bars represent the standard deviation for 3 samples. (e and f) Plots of log (current) versus log (scan rate) showing two regimes at slow (5–50 mV/s) and fast (100–500 mV/s) scan rates. Calculated *b* values using eq 2 are tabulated in Table 2.

Grazing incidence X-ray diffraction (GIXRD) data were acquired for three films: (1) a spin-coated colloidal solution, (2) an as-deposited NbO_x film, and (3) a calcined Nb_2O_5 films (550 °C × 5 h in air) (Figure 4c). Samples 1 and 2 showed no crystallinity (line at 38° and 45° are assigned to the gold substrate), but sample 3 produced reflections all of which were assignable to orthorhombic, *T*-Nb_2O_5 (JCPDS 30-873). Scherrer analysis[32] of the line widths affords an estimate of

DOI: 10.1021/acs.chemmater.8b03254
Chem. Mater. XXXX, XXX, XXX−XXX

Table 2. Metrics for T-Nb_2O_5 Films Synthesized by ED

charge (mC)	mass (μg)	thickness (nm)	C_{sp} at 5 mV/s (F/g)	C_{sp} at 5 A/g (mAh/g)	CV cycles[a] at 200 mV/s	galvanostatic cycles[b] at 10 A/g
300	1.85	38	1255.7 ± 375.2	560.5 ± 167.5	1200	200
500	3.09	60	977.2 ± 45.7	424.6 ± 19.9	2800	>500
1000	6.18	102	892.7 ± 133.7	251.5 ± 37.7	2000	300
1500	9.27	144	679.0 ± 56.0	230.0 ± 18.9	1000	>500

[a]Cycles to 20% capacity fade. [b]Cycles to 20% capacity fade.

the grain size for these films of 19.3 nm, calculated using the (001), (181) and (002) reflections. Quartz crystal microbalance gravimetry (QCM) was used to measure the mass of the dried films which increased in direct proportion to the Coulombic loading, Q_{dep}, yielding a slope of 6.18 μg/C (Figure 4d). The film thickness, measured by AFM, also increased in proportion to Q_{dep} (Figure 4, panels e and f). The range of Q_{dep} values explored in this study corresponded to film thickness ranging from 38 nm (300 mC) to 144 nm (1500 mC).

Cyclic voltammetry (CV). The electrochemical properties of T-Nb_2O_5 film half-cells were investigated in dry, 1.0 M $LiClO_4$, propylene carbonate electrolyte using a three-electrode cell with a nonaqueous Ag/Ag^+ reference electrode and Pt counter electrodes. In the following discussion and figures, we convert these potentials to Li/Li^+ (+3.04 V vs NHE) for convenience. Cyclic voltammograms (CVs) for a 1.8 V window from 1.5 to 3.3 V versus Li/Li^+ are shown at scan rates of 5, 100, and 500 mV/s for all four films (Figure 5, panels a, b, and c).

The theoretical Faradaic capacity of Nb_2O_5 is 726 C/g assuming x = 2.0 in eq 1.[7] This corresponds to a specific capacitance, C_{sp} = 202 mAh/g or 403 F/g for the 1.8 V window measured in Figure 5. All four T-Nb_2O_5 films produce C_{sp} values considerably higher than this at 5 mV/s, ranging from 600 to 1250 F/g (Figure 5d and Table 2). In order for the measured specific capacity to be higher than the theoretical Faradaic capacity, charge must be stored by a non-Faradaic mechanism. Double-layer charging of the film is the most likely candidate for this mechanism. As shown in Figure 5d, C_{sp} is rapidly lost with increasing scan rate above 5 mV/s. But the retention of capacity at higher scan rates is very good, with the thinnest of these films (Q_{dep} = 300 mC, d = 38 nm) exhibiting the theoretical Faradaic capacity at a scan rate of 500 mV/s (Figure 5d).

A closer look at the CV data allows the influence of Li^+ transport on C_{sp} to be better understood. The cyclic voltammetric peak current, i_p, shows a scan rate, ν, dependence given by[26]

$$i_p = a\nu^b \tag{3}$$

where a is a constant and the value of b provides insight into whether diffusional transport limits the measured i_p. b = 0.5 signifies a diffusion-controlled current, whereas b = 1.0 is produced by diffusion-independent processes which could be non-Faradaic (e.g., capacitive charging) or Faradaic (e.g., pseudocapacitive), provided ion transport is rapid enough.[26] In the thinnest T-Nb_2O_5 films examined here (Q_{dep} = 300 mC, d = 38 nm), b approaches 1.0 at slow scan rates (5−50 mV/s, Figure 5, panels e and f), suggesting that the diffusion of Li^+ within these films is sufficiently rapid to enable all Nb centers to be charge-compensated on the time scale of a single voltammetric scan. For example, at ν = 20 mV/s, $\tau_{CV} \approx RT/F\nu$ = 1.3 s,[26] where R, T, and F are the gas constant, the temperature, and Faraday's constant, respectively. Since $n \approx$ 1.0 (Figure 5, panels e and f), the film is behaving pseudocapacitively, implying that Li^+ is able to access the entire 38 nm T-Nb_2O_5 film. This requires that $D_{Li^+} \geq d^2/2\tau_{CV} = 6 \times 10^{-12}$ cm^2/s.[26] As d increases from 38 to 140 nm (Q_{dep} = 1500 mC), b decreases from ∼0.95 to ∼0.75 in this slow scan rate regime, suggesting that Li^+ diffusion is no longer able to access all Nb centers, and the Faradaic current is increasing diffusion-limited (b = 0.5).

At scan rates of 100 mV/s and above, T-Nb_2O_5 films of all four thickness show lower b values in the 0.36−0.67 range (Figure 5, panels e and f, and Table 3). Notably, b values even

Table 3. b-Values[a] for Nb_2O_5 Films as a Function of Deposition Charge

	Q_{dep}[b] (mC)	slow scan rates (5−50 mV/s)	fast scan rates (100−500 mV/s)
anodic	300	b = 0.94	b = 0.67
	500	0.82	0.6
	1000	0.8	0.42
	1500	0.79	0.36
cathodic	300	b = 0.96	b = 0.65
	500	0.89	0.59
	1000	0.76	0.44
	1500	0.74	0.39

[a]b-Value, as defined by eq 2. [b]Nb_2O_5 ED deposition charge at a 6 × 6 mm FTO electrode with area 0.36 cm^2.

lower than 0.5 are observed for the thickest films, indicating that uncompensated ohmic resistance and/or rate-limiting electron transfer act to limit the current in addition to Li^+ diffusion.[26] In this fast scan rate regime, thinner films are storing charge both capacitively (n = 1.0) and by accessing Nb centers via Li^+ diffusion (n = 0.5), but the entire film thickness is not accessible to Li^+ on these time scales. For example, if Li^+ transport is diffusion-controlled within the 38 nm film, this requires that $D_{Li^+} \leq d^2/2\tau_{CV} = 1.4 \times 10^{-10}$ cm^2/s. Thus, the cyclic voltammetric behavior of the 38 nm sample can be understood if D_{Li^+} satisfies this inequality: 6×10^{-12} cm^2/s < D_{Li^+} < 1.4×10^{-10} cm^2/s, or approximately 10^{-11} cm^2/s. This D_{Li^+} value is in the range of other transition metal oxides used for Li^+ storage.[33−37]

At ν = 500 mV/s the cyclic voltammograms for all four films converge (Figure 5c). This behavior is expected if τ_{CV} limits Li^+ diffusion to distances smaller than the thickness of all four films. In this limit, Li^+ is able to access the same volume, and the same number of Nb centers, for all four films. At 500 mV/s, $\tau_{CV} \approx$ 50 ms.

As already noted, the C_{sp} measured by cyclic voltammetry at slow scan rates is higher than the theoretical Faradaic C_{sp} value of 403 F/g (1.8 V window). This implies that non-Faradaic

DOI: 10.1021/acs.chemmater.8b03254
Chem. Mater. XXXX, XXX, XXX−XXX

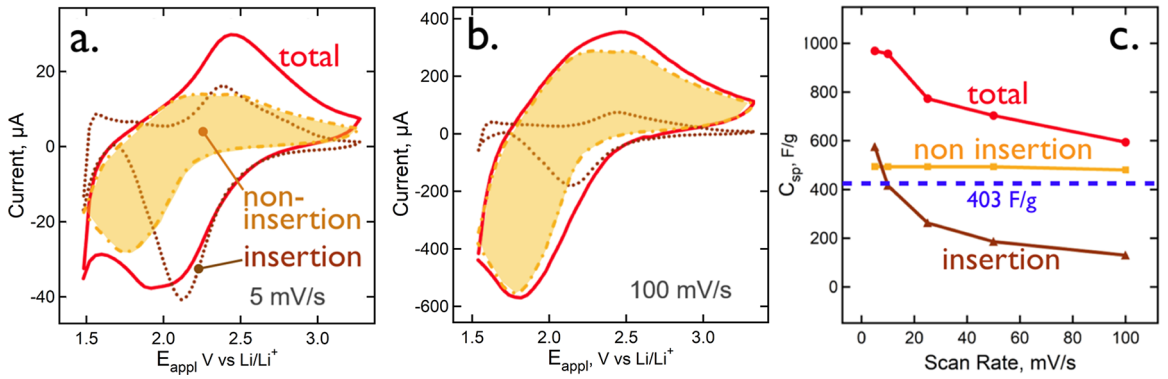

Figure 6. Deconvolution of insertion and noninsertion currents in a cyclic voltammogram using the method of Conway.[38] (a) CV at 5 mV/s for a 500 mC *T*-Nb_2O_5 film. (b) CV for the same film at 100 mV/s. (c) Plot of total C_{sp}, together with the insertion and noninsertion capacities as a function of scan rate, ν. The dash blue line marks the theoretical Faradaic capacity, 403 F/g for a 1.8 V window.

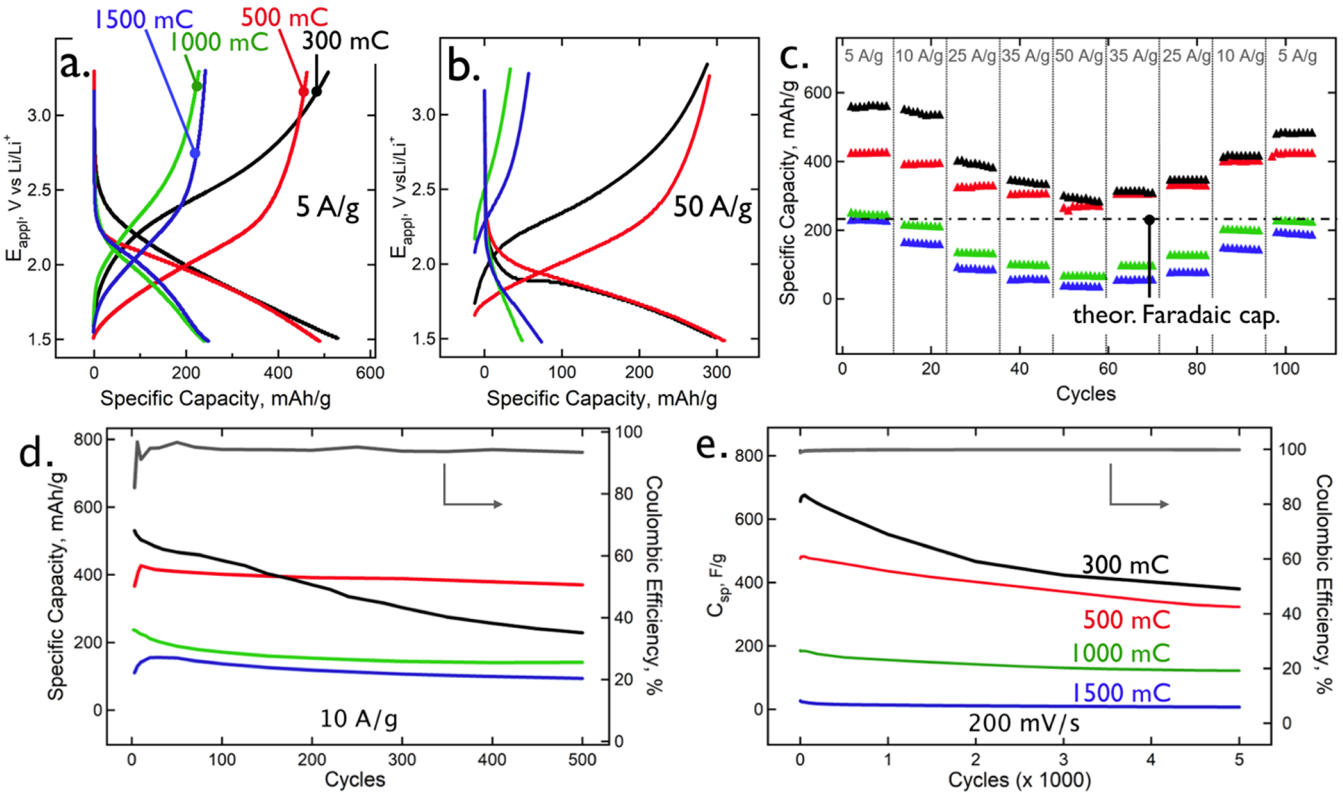

Figure 7. Galvannostatic charge/discharge and assessments of cycle stability. (a and b) Galvannostatic charge−discharge curves for rates of (a) 5A/g and (b) 50 A/g. (c) Measurements of specific capacity for all four film thicknesses at five galvannostatic rates ranging from 5 to 50 A/g. (d) Cycle stability of C_{sp} for galvannostatic charge/discharge across 500 cycles. (e) Cycle stability of C_{sp} for cyclic voltammetric charge/discharge at 200 mV/s across a 1.8 V window and 5000 cycles.

energy storage contributes substantially to the measured C_{sp}, but what experimental evidence supports the existence of this double-layer capacity? A version of eq 3 can be used to resolve the total current into insertion and noninsertion components, the latter of which includes double-layer charging as well as the Faradaic capacity of the *T*-Nb_2O_5 surface.[38−40] The total current at any potential and scan rate, ν, can be written as[38−40]

$$i(\nu) = k_1\nu + k_2\nu^{1/2} \quad (4)$$

where the first term accounts for the noninsertion current (i.e., nondiffusion controlled), the second term is the insertion current (diffusion-controlled), and k_1 and k_2 are scan rate independent constants. A plot of the quotient $[i(\nu)/\nu^{1/2}]$ versus $\nu^{1/2}$ at each potential point yields the values of k_1 and k_2 as the slope and intercept, respectively.[38−40] Application of this deconvolution algorithm to a 500 mC *T*-Nb_2O_5 film (Figure 6) allows the insertion and noninsertion currents to be plotted separately, together with the total current (Figure 6, panels a and b). At ν = 5 mV/s, a large noninsertion current is observed that is similar in magnitude to the insertion current (Figure 6a), and at 100 mV/s, the noninsertion capacity dominates (Figure 6b). The fraction of the total capacity, C_{sp}, comprised by insertion decreases smoothly with ν from 55% at 5 mV/s to 19% at 100 mV/s (Figure 6c). This analysis suggest that a large noninsertion capacity that rivals or exceeds the insertion capacity operates in these ED T-Nb_2O_5 films, providing a

DOI: 10.1021/acs.chemmater.8b03254
Chem. Mater. XXXX, XXX, XXX−XXX

Table 4. Literature Review of Energy Storage Metrics for Nb_2O_5 Films[a]

material	synthesis method	film thickness	voltage window (V)	sp. energy (Wh/kg)	sp. power (kW/kg)	cycle stability	ref
Nb_2O_5@CNTs	HT	3 μm	1.5	450-355	1.1−8.5		1
Nb_2O_5@CDC	HT	70 μm	1.8	158-130	0.9−3.6		4
T-Nb_2O_5	HT	40 μm	1.8	252-87	0.3−86		13
ox. Nb_2CT_x	HT	50 μm	1.8	133-30	0.13−6		3
np Nb_2O_5	A&A	250 μm	2.0	475-322	0.1−1.6		45
o-Nb_2O_5@C	HT	50 μm	2.0	278-117	2−100		46
Nb_2O_5 nb	HT	15 nm	1.8	450-150	0.2−180		41
T-Nb_2O_5							
Q_{dep} = 500 mC	ED	60 nm	1.8	770-486	9−90		this work
Q_{dep} = 1000 mC	ED	100 nm	1.8	421-84	9−90		this work

[a]Abbreviations: ox = oxidized, np = nanoporous, nb = nanobelts, A&A = anodization and thermal annealing, HT = hydrothermal, ED = electrophoretic deposition, CNT = carbon nanotubes, CDC = carbide-derived carbon, *T*-Nb_2O_5 = orthorhombic Nb_2O_5, Nb_2CT_x = 2D niobium carbide MXene, and *o*-Nb_2O_5@carbon = orthorhombic-Nb_2O_5@carbon core−shell microspheres.

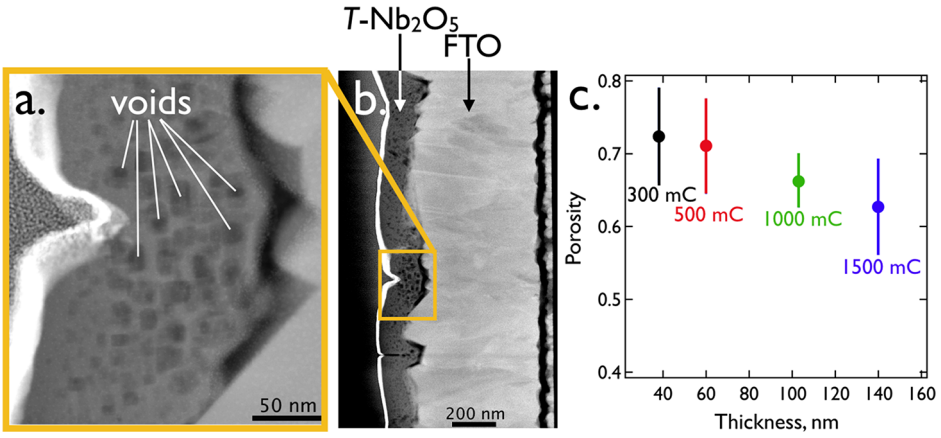

Figure 8. *T*-Nb_2O_5 film porosity. (a and b) Cross-sectional images of a 140 nm *T*-Nb_2O_5 film prepared with Q_{dep} = 1500 mC. The porosity of *T*-Nb_2O_5 films prepared by ED of 72%−64% is attributed to voids within the bulk of the *T*-Nb_2O_5 film seen in these high-angle annular dark field (HAADF)-STEM images. (c) Calculated porosity versus thickness for *T*-Nb_2O_5 films, derived from AFM measurements of thickness and QCM measurements of the mass of each film.

mechanism for this material to achieve a total C_{sp} value that is up to twice the theoretical Faradaic value.

Galvanostatic Charge/Discharge and Assessments of Cycle Stability. Galvanostatic charge/discharge curves for *T*-Nb_2O_5 films, evaluated at 5−50 A/g, show appreciable capacity for these films even at 50 A/g (Figure 6, panels a−c). For example, 300 mC films (d = 38 nm) produce C_{sp} approaching ~300 mAh/g, whereas 1000 mC and 1500 mC films (100, and 140 nm) show C_{sp} of 40−60 mAh/g at a 50 A/g rate (Figure db). For the 500 mC sample (d = 60 nm), C_{sp} exceeds 400 mAh/g at 10 A/g, which translates to an energy density of >700 Wh/kg, at a power density of 18 kW/kg (Figure 6c). As indicated in Figure 6c, the two thinnest films exceed the theoretical Faradaic capacity of Nb_2O_5 of 202 mAh/g even at 50 A/g. As discussed in greater detail below, this requires the participation of non-Faradaic charge storage in the form of double-layer charging (Figure 7).

The cycle stability of charge storage is critically important for all technological applications of energy storage materials. In prior work (Table 4), Zhou[41] reported Nb_2O_5 nanobelts (15 × 60 nm in width) produced C_{sp} values of 50 mAh/g and showed virtually no fade for 50 cycles. Zhang and co-workers[42] demonstrated Nb_2O_5 nanoparticle/CNT composites that demonstrated 128 mAh/g at a 5 A/g rate for 2000 cycles with 95% retention of this capacity. Extraordinary cycle stability of *T*-Nb_2O_5 nanoparticle-decorated carbon fibers was reported by Yun and co-workers[43] who achieved C_{sp} values in the range from 240−356 F/g (0.5−10 A/g) and cycle stabilities to 70000 cycles, unfortunately, at an unspecified rate. Dunn and co-workers[1] studied the same composite system and reported 500 cycles with 5% fade at 380 C/g (80 mAh/g) cycled at a 20 C rate. These examples, which are representative of the best in terms of demonstrating excellent cycle stability of Nb_2O_5, all involve nanostructures or dispersions of Nb_2O_5 nanoparticles on a conductive support.

T-Nb_2O_5 films represent a much different type of sample. Since voltage cycling and galvannostatic cycling can produce very different results for the same material, we investigated both (Figure 8). All four films were cycled at 10 A/g for 500 cycles (Figure 6d) and, with different samples, across 1.8 V at 200 mV/s for up to 10000 cycles (5000 shown in Figure 6e). These are amongst the highest rates at which stability has been tested for this material, to our knowledge. Galvanostatic cycling under these conditions often resulted in little measurable capacity fade (Figure 6d, Q_{dep} = 1500, 1000, and 500 mC samples), but significant fade (55%) was also seen for some samples (e.g., Figure 6d, Q_{dep} = 300 mC). These trends are representative of a larger number of samples examined in this study. *T*-Nb_2O_5 films exhibited significantly better stability in CV cycling (Figure 6e) where films retained in excess of 60% of their initial C_{sp} to 5000 cycles, and more than 40% to 10000 cycles.

DOI: 10.1021/acs.chemmater.8b03254
Chem. Mater. XXXX, XXX, XXX−XXX

Mesoporosity in ED T-Nb_2O_5 Films. The nanometer-scale thicknesses of the *T*-Nb_2O_5 film studied here precluded the measurement of specific surface areas using the BET method. But porosity data were acquired directly, by measuring the apparent density of the film, ρ_{expt}, based upon the AFM-measured film thickness, *d*, and the QCM-measured film dry mass, *m*. In conjunction with the known density of Nb_2O_5, ρ_{theor}, a porosity is obtained (Figure 7c):

$$\text{porosity} = 1.0 - \frac{\rho_{exptl}}{\rho_{theor}} \quad (5)$$

The measured values, ranging from 72% for the 300 mC (*d* = 38 nm) film to 64% for the 1500 mC (140 nm) film, are surprisingly large.

This porosity can be directly imaged by STEM in cross-sectional thin sections of these films (Figure 7, panels a and b). These images show many spherical voids (dark regions in these dark field images) within the *ED T*-Nb_2O_5 matrix. These voids range in diameter from 1−10 nm where smaller voids (diameter 1−2 nm) are uniformly distributed, but larger voids (8−10 nm) tend to form clusters (one of these is shown in Figure 7b). This mesoporosity provides an explanation for the large noninsertion capacities demonstrated in Figure 6. Both the double-layer capacity and the surface Faradaic capacities are proportional to the wetted surface area of the film.

How do these voids form? Our hypothesis is that hydrogen nanobubbles that coevolve during the ED process (macroscopic H_2 bubbles are also seen on the electrode surface during ED) adhere to the nascent NbO_x film and are covered and encapsulated by NbO_x colloids during the ED growth process. Confirmation of this mechanism must await further experimentation; however, if this mechanism is correct, it could provide a means for controlling the mesoporosity of these films by adjusting the rate of H_2 evolution during the ED process.

SUMMARY

The electrochemical preparation of high quality, crystalline *T*-Nb_2O_5 thin films can be achieved using the ED process described here. This method affords control of film thickness from 38 to 140 nm. Moreover, these ED T-Nb_2O_5 films achieve capacities for Li^+ storage of ≈1200 F/g at 5 mV/s (1.8 V window) and 610 F/g at 100 mV/s that exceed the theoretical Faradaic capacities for this material (403 F/g) and are unprecedented to our knowledge. A Ragone plot for two of these films (Figure 9) is compared with prior work on Nb_2O_5, highlighting the excellent energy storage performance of these ED films.

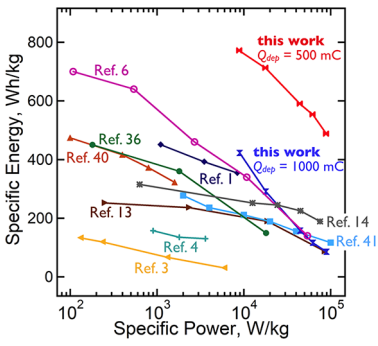

Figure 9. Ragone plot for comparison of the half-cell performance for *T*-Nb_2O_5 films prepared using ED with literature results. Data for Q_{dep} = 500 mC and Q_{dep} = 1000 mC represent the average measured for three independent samples.

These exceptional C_{sp} values are attributed to a significant porosity of ≈70% that enables a large double-layer capacity that is 50% of C_{sp} at 5 mV/s and 80% at 100 mV/s. This capacity is sustainable for many charge−discharge cycles, with 500 mC films retaining a C_{sp} of 350 F/g to 5000 cycles. A similar trend is observed in the galvanostatic charge−discharge, where high energy densities of ≈700 Wh/kg are obtained at power densities as high as 18 kW/kg.

AUTHOR INFORMATION

Corresponding Authors

*E-mail: xpan@uci.edu.

*E-mail: rmpenner@uci.edu.

ORCID

Sheng Dai: 0000-0001-5787-0179

Xiaoqing Pan: 0000-0002-0965-8568

Reginald M. Penner: 0000-0003-2831-3028

Notes

The authors declare no competing financial interest.

ACKNOWLEDGMENTS

This work was supported by Nanostructures for Electrical Energy Storage (NEES II), an Energy Frontier Research Center (EFRC) funded by the U.S. Department of Energy, Office of Science, Office of Basic Energy Sciences under award number DESC0001160. Valuable discussions with Professor Phil Collins, Professor Zuzanna Siwy, Professor Bruce Dunn, and their students are gratefully acknowledged. SEM, TEM, XRD, and XPS data were acquired at the Irvine Materials Research Institute (*IMRI*, imri.uci.edu) at UCI.

REFERENCES

(1) Wang, X.; Li, G.; Chen, Z.; Augustyn, V.; Ma, X.; Wang, G.; Dunn, B.; Lu, Y. High-Performance Supercapacitors Based on Nanocomposites of Nb_2O_5 Nanocrystals and Carbon Nanotubes. *Adv. Energy Mater.* **2011**, *1*, 1089−1093.

(2) Kim, J. W.; Augustyn, V.; Dunn, B. The Effect of Crystallinity on the Rapid Pseudocapacitive Response of Nb_2O_5. *Adv. Energy Mater.* **2012**, *2*, 141−148.

(3) Zhang, C.; Beidaghi, M.; Naguib, M.; Lukatskaya, M.; Zhao, M.; Dyatkin, B.; Cook, K.; Kim, S.; Eng, B.; Xiao, X.; Gogotsi, Y.; Long, D.; Qiao, W.; Dunn, B. Synthesis and Charge Storage Properties of Hierarchical Niobium Pentoxide/Carbon/Niobium Carbide (MXene) Hybrid Materials. *Chem. Mater.* **2016**, *28*, 3937−3943.

(4) Zhang, C.; Maloney, R.; Lukatskaya, M.; Beidaghi, M.; Dyatkin, B.; Perre, E.; Long, D.; Qiao, W.; Dunn, B.; Gogotsi, Y. Synthesis and Electrochemical Properties of Niobium Pentoxide Deposited on Layered Carbide-Derived Carbon. *J. Power Sources* **2015**, *274*, 121−129.

(5) Lim, E.; Kim, H.; Jo, C.; Chun, J.; Ku, K.; Kim, S.; Lee, H.; Nam, I.-S.; Yoon, S.; Kang, K.; Lee, J. Advanced Hybrid Supercapacitor Based on a Mesoporous Niobium Pentoxide/Carbon as High-Performance Anode. *ACS Nano* **2014**, *8*, 8968−8978.

(6) Zhao, G.; Ye, C.; Zhang, L.; Li, C.; Sun, K. *T*-Nb2O5 quantum dots prepared by electrodeposition for fast Li ion intercalation/deintercalation. *Nanotechnology* **2017**, *28*, 215401.

(7) Ohzuku, T.; Sawai, K.; Hirai, T. Electrochemistry of L-niobium Pentoxide A Lithium/Non-Aqueous Cell. *J. Power Sources* **1987**, *19*, 287−299.

DOI: 10.1021/acs.chemmater.8b03254
Chem. Mater. XXXX, XXX, XXX−XXX

(8) Gomes, M. A.; Bulhões, L. O. d. S.; De Castro, S. C.; Damião, A. J. The Electrochromic Process at Nb_2O_5 Electrodes Prepared by Thermal Oxidation of Niobium. *J. Electrochem. Soc.* **1990**, *137*, 3067−3070.
(9) Schmitt, M.; Heusing, S.; Aegerter, M.; Pawlicka, A.; Avellaneda, C. Electrochromic Properties of Nb_2O_5 Sol−Gel Coatings. *Sol. Energy Mater. Sol. Cells* **1998**, *54*, 9−17.
(10) Rosario, A.; Pereira, E. Optimisation of the Electrochromic Properties of Nb_2O_5 Thin Films produced by Sol−Gel route using Factorial Design. *Sol. Energy Mater. Sol. Cells* **2002**, *71*, 41−50.
(11) Huang, Y.; Zhang, Y.; Hu, X. Structural, Morphological and Electrochromic Properties of Nb_2O_5 Films Deposited by Reactive Sputtering. *Sol. Energy Mater. Sol. Cells* **2003**, *77*, 155−162.
(12) Coşkun, Ö. D.; Demirel, S.; Atak, G. The Effects of Heat Treatment on Optical, Structural, Electrochromic and Bonding Properties of Nb_2O_5 Thin Films. *J. Alloys Compd.* **2015**, *648*, 994−1004.
(13) Augustyn, V.; Come, J.; Lowe, M. A.; Kim, J. W.; Taberna, P.-L.; Tolbert, S. H.; Abruña, H. D.; Simon, P.; Dunn, B. High-rate electrochemical energy storage through Li+ intercalation pseudocapacitance. *Nat. Mater.* **2013**, *12*, 518.
(14) Lai, C.-H.; Ashby, D.; Moz, M.; Gogotsi, Y.; Pilon, L.; Dunn, B. Designing Pseudocapacitance for Nb_2O_5/Carbide-Derived Carbon Electrodes and Hybrid Devices. *Langmuir* **2017**, *33*, 9407−9415.
(15) Griffith, K. J.; Forse, A. C.; Griffin, J. M.; Grey, C. P. High-rate Intercalation without Nanostructuring in Metastable Nb_2O_5 Bronze phases. *J. Am. Chem. Soc.* **2016**, *138*, 8888−8899.
(16) Le Viet, A.; Jose, R.; Reddy, M.; Chowdari, B.; Ramakrishna, S. Nb_2O_5 Photoelectrodes for Dye-Sensitized Solar Cells: Choice of the Polymorph. *J. Phys. Chem. C* **2010**, *114*, 21795−21800.
(17) Romero, R.; Ramos-Barrado, J.; Martin, F.; Leinen, D. Nb_2O_5 Thin Films Obtained by Chemical Spray Pyrolysis. *Surf. Interface Anal.* **2004**, *36*, 888−891.
(18) Özer, N.; Rubin, M. D.; Lampert, C. M. Optical and Electrochemical Characteristics of Niobium Oxide Films prepared by Sol-Gel Process and Magnetron Sputtering: A Comparison. *Sol. Energy Mater. Sol. Cells* **1996**, *40*, 285−296.
(19) Viet, A. L.; Reddy, M.; Jose, R.; Chowdari, B.; Ramakrishna, S. Nanostructured Nb_2O_5 Polymorphs by Electrospinning for Rechargeable Lithium Batteries. *J. Phys. Chem. C* **2010**, *114*, 664−671.
(20) Lee, G.; Crayston, J. Studies on the Electrochemical Deposition of Niobium Oxide. *J. Mater. Chem.* **1996**, *6*, 187−192.
(21) Zhitomirsky, I. Electrolytic Deposition of Niobium Oxide Films. *Mater. Lett.* **1998**, *35*, 188−193.
(22) Zhitomirsky, I.; Gal-Or, L.; Kohn, A.; Hennicke, H. Electrodeposition of Ceramic Films from Non-Aqueous and Mixed Solutions. *J. Mater. Sci.* **1995**, *30*, 5307−5312.
(23) Gomes, M. B.; Onofre, S.; Juanto, S.; Bulhoes, L. d. S. Anodization of Niobium in Sulphuric Acid Media. *J. Appl. Electrochem.* **1991**, *21*, 1023−1026.
(24) Zhiyu, Q.; Pierre, T. Electrochemical Reduction of Niobium Ions in Molten LiF-NaF. *J. Appl. Electrochem.* **1985**, *15*, 259−265.
(25) Chong, N.-S.; Anderson, J. L.; Norton, M. L. Nonaqueous Electrodeposition of Niobium from Propylene Carbonate and Acetonitrile. *J. Electrochem. Soc.* **1989**, *136*, 1245−1246.
(26) Bard, A. J.; Faulkner, L. R. *Electrochemical Methods: Fundamentals and Applications*, 2nd ed.; Wiley: New York, 2001.
(27) Laoire, C. O.; Plichta, E.; Hendrickson, M.; Mukerjee, S.; Abraham, K. Electrochemical Studies of Ferrocene in a Lithium Ion Conducting Organic Carbonate Electrolyte. *Electrochim. Acta* **2009**, *54*, 6560−6564.
(28) Sauerbrey, G. Use of Quartz Crystal Units for Weighing Thin Films and Microweighing. *Eur. Phys. J. A* **1959**, *155*, 206−222.
(29) Gabrielli, C.; Keddam, M.; Torresi, R. Calibration of the Electrochemical Quartz Crystal Microbalance. *J. Electrochem. Soc.* **1991**, *138*, 2657−2660.
(30) Yan, W.; Kim, J. Y.; Xing, W.; Donavan, K. C.; Ayvazian, T.; Penner, R. M. Lithographically Patterned Gold/Manganese Dioxide Core/Shell Nanowires for High Capacity, High Rate, and High Cyclability Hybrid Electrical Energy Storage. *Chem. Mater.* **2012**, *24*, 2382−2390.
(31) Avellaneda, C. O.; Pawlicka, A. Two Methods of Obtaining Sol−Gel Nb_2O_5 Thin Films for Electrochromic Devices. *J. Mater. Sci.* **1998**, *33*, 2181−2185.
(32) Patterson, A. The Scherrer Formula for X-ray Particle Size Determination. *Phys. Rev.* **1939**, *56*, 978−982.
(33) Van der Ven, A.; Bhattacharya, J.; Belak, A. A. Understanding Li diffusion in Li-intercalation compounds. *Acc. Chem. Res.* **2013**, *46*, 1216−1225.
(34) Prosini, P. P.; Lisi, M.; Zane, D.; Pasquali, M. Determination of the Chemical Diffusion Coefficient of Lithium in LiFePO4. *Solid State Ionics* **2002**, *148*, 45−51.
(35) Aurbach, D.; Levi, M. D.; Levi, E.; Teller, H.; Markovsky, B.; Salitra, G.; Heider, U.; Heider, L. Common Electroanalytical Behavior of Li Intercalation Processes into Graphite and Transition Metal Oxides. *J. Electrochem. Soc.* **1998**, *145*, 3024−3034.
(36) Kang, K.; Ceder, G. Factors That Affect Li Mobility in Layered Lithium Transition Metal Oxides. *Phys. Rev. B: Condens. Matter Mater. Phys.* **2006**, *74*, 094105.
(37) Sun, Y.-K.; Chen, Z.; Noh, H.-J.; Lee, D.-J.; Jung, H.-G.; Ren, Y.; Wang, S.; Yoon, C. S.; Myung, S.-T.; Amine, K. Nanostructured High-Energy Cathode Materials for Advanced Lithium Batteries. *Nat. Mater.* **2012**, *11*, 942.
(38) Liu, T.-C.; Pell, W.; Conway, B.; Roberson, S. Behavior of molybdenum nitrides as materials for electrochemical capacitors comparison with ruthenium oxide. *J. Electrochem. Soc.* **1998**, *145*, 1882−1888.
(39) Wang, J.; Polleux, J.; Lim, J.; Dunn, B. Pseudocapacitive Contributions to Electrochemical Energy Storage in TiO_2 (Anatase) Nanoparticles. *J. Phys. Chem. C* **2007**, *111*, 14925−14931.
(40) Brezesinski, K.; Wang, J.; Haetge, J.; Reitz, C.; Steinmueller, S. O.; Tolbert, S. H.; Smarsly, B. M.; Dunn, B.; Brezesinski, T. Pseudocapacitive Contributions to Charge Storage in Highly Ordered Mesoporous Group V Transition Metal Oxides with Iso-Oriented Layered Nanocrystalline Domains. *J. Am. Chem. Soc.* **2010**, *132*, 6982−6990.
(41) Wei, M.; Wei, K.; Ichihara, M.; Zhou, H. Nb_2O_5 Nanobelts: A lithium Intercalation Host with Large Capacity and High Rate Capability. *Electrochem. Commun.* **2008**, *10*, 980−983.
(42) Luo, G.; Li, H.; Zhang, D.; Gao, L.; Lin, T. A Template-free Synthesis via Alkaline route for Nb_2O_5/carbon Nanotubes Composite as Pseudo-capacitor Material with High-Rate Performance. *Electrochim. Acta* **2017**, *235*, 175−181.
(43) Song, M. Y.; Kim, N. R.; Yoon, H. J.; Cho, S. Y.; Jin, H.-J.; Yun, Y. S. Long-lasting Nb_2O_5-based Nanocomposite materials for Li-ion storage. *ACS Appl. Mater. Interfaces* **2017**, *9*, 2267−2274.
(44) Teixeira da Silva, V. L. S.; Schmal, M.; Oyama, S. Niobium Carbide Synthesis from Niobium Oxide: Study of the Synthesis Conditions, Kinetics, and Solid-State transformation Mechanism. *J. Solid State Chem.* **1996**, *123*, 168−182.
(45) Rahman, M. M.; Rani, R. A.; Sadek, A. Z.; Zoolfakar, A. S.; Field, M. R.; Ramireddy, T.; Kalantar-Zadeh, K.; Chen, Y. A Vein-Like Nanoporous Network of Nb_2O_5 with a Higher Lithium Intercalation Discharge Cut-Off Voltage. *J. Mater. Chem. A* **2013**, *1*, 11019−11025.
(46) Kong, L.; Zhang, C.; Wang, J.; Qiao, W.; Ling, L.; Long, D. Nanoarchitectured Nb_2O_5 Hollow, Nb_2O_5@ Carbon and NbO_2@ Carbon Core-Shell Microspheres for Ultrahigh-Rate Intercalation Pseudocapacitors. *Sci. Rep.* **2016**, *6*, 21177.

DOI: 10.1021/acs.chemmater.8b03254
Chem. Mater. XXXX, XXX, XXX−XXX